Materials Advances

PAPER

Cite this: *Mater. Adv.*, 2024, 5, 5514

Efficient photo-oxidation of bisphenol a and tetracycline through sulfur-doped g-C_3N_4/CD heterojunctions†

Ankoor Sura,[a] Amanvir Singh,[a] Arjun Singh,[a] Sudha Narwal,[a] Priya Malik,[b] Manjeet Singh Goyat,[c] Yogendra K. Mishra,[d] Sonia Nain*[a] and Surender Duhan*[b]

Received 15th March 2024,
Accepted 16th May 2024

DOI: 10.1039/d4ma00270a

rsc.li/materials-advances

The synergistic effects of sulfur-doped g-C_3N_4 (SCN) and carbon dots (CD) in nanocomposite photocatalysts were explored for the degradation of contaminants of emerging concern (CECs), particularly phenolic pollutants such as bisphenol A (BPA) and tetracycline (TC). Various SCN/CD nanocomposites were synthesized *via* thermal polymerization by mixing with different CD concentrations with thiourea (1, 2, 3, and 4 by wt%), denoted as SCN/CD1, SCN/CD2, SCN/CD3, and SCN/CD4, respectively. The embedded CD functions as an intrinsic surface modifier on the surface of the SCN which facilitated the suppression of electron–hole recombination and promoted photocatalytic activity. Among the synthesized catalysts, SCN/CD3 exhibited remarkable efficiency, degrading a 50-ppm solution of BPA to 92.5% and TC to 90.7% within 60 minutes, utilizing 50 mg of catalyst. Moreover, SCN/CD3 demonstrated exceptional reusability over five cycles without significant degradation in efficiency. Radical scavenging experiments identified holes (h^+) and superoxide radicals ($O_2^{\bullet-}$) as the primary radical species responsible for pollutant degradation. This work highlights the potential of SCN/CD composite photocatalysts in solving water pollution concerns by elucidating a promising photocatalytic degradation process for CECs.

1. Introduction

The escalating global demand for water resources has accentuated the need for effective water and wastewater treatment technologies. However, despite progress in traditional treatment methods, the prevalence of contaminants of emerging concern (CECs) poses a formidable challenge.[1,2] These CECs, encompassing a spectrum of pollutants from pharmaceuticals[3] to endocrine disruptors, persist in water sources, posing significant threats to both the environment and human health. Among the myriad of CECs, bisphenol A (BPA)[4,5] and tetracycline (TC)[6–8] stand out due to their widespread presence and potential adverse effects. BPA, a ubiquitous component of plastic products,[9] and TC, a common antibiotic, are prevalent in various industrial effluents and municipal wastewater streams. Alarmingly, the concentrations of TC in pharmaceutical wastewater can soar to staggering levels, reaching up to 1077 mg L^{-1},[10,11] while BPA concentrations in landfill leachate and industrial effluents range from 0.37 to 17.2 mg L^{-1}.[12,13] Such elevated concentrations underscore the urgency to devise efficient remediation strategies to mitigate their detrimental impacts.

Photocatalysis stands as a beacon of hope in the realm of environmental remediation and clean energy production, offering a green and sustainable solution to pressing global challenges.[14] Graphitic carbon nitride (g-C_3N_4)[15] is one of the several types of photocatalysts that has drawn interest since it is devoid of metals and reacts to visible light making it appropriate for a variety of uses, such the evolution of hydrogen or oxygen,[16,17] CO_2 reduction,[18] and environmental remediation.[19] However, bulk g-C_{3GC} faces limitations including high defect density, fast charge recombination, and low specific surface area.[20] To address these challenges, researchers

---

[a] Department of Chemistry, Deenbandhu Chhotu Ram University of Science and Technology, Murthal-131039, Haryana, India. E-mail: sonianain.chem@dcrustm.org
[b] Advanced Sensors Lab, Department of Physics, Deenbandhu Chhotu Ram University of Science and Technology, Murthal-131039, Haryana, India. E-mail: surender6561@gmail.com
[c] Department of Applied Science, University of Petroleum and Energy Studies, Dehradun, Uttarakhand, India
[d] Syddansk Universitet-Campus Sonderborg, NanoSYD, Mads Clausen Institute, Sonderborg, Denmark

† Electronic supplementary information (ESI) available: Supplementary information includes degradation pathway for BPA and TC evaluated through LCMS, degradation efficiency after repeated experiment and atomic % of elements detected by XPS. See DOI: https://doi.org/10.1039/d4ma00270a

have explored sensitized doping as a strategy to boost the photocatalytic activity of g-C_3N_4.[21] Structural defects are created in the g-C_3N_4 lattice by adding non-metallic elements like sulphur, which optimises the electron distribution and changes the band gap location.[22] This facilitates charge transfer at the material interface, expands light absorption range, and promotes efficient electron–hole separation, thus enhancing overall efficiency. Sulfur-doped g-C_3N_4 (SCN) exhibits superior photocatalytic activity compared to other dopants, owing to its improved specific surface area, enhanced light utilization rate, and superior efficiency of electron–hole separation.[23,24] Additionally, it serves as an excellent carrier in heterojunction structure construction, facilitating charge separation and providing additional binding sites for pollutant adsorption.

Furthermore, the presence of carbon dots (CD) in g-C_3N_4 nanocomposites can facilitate interfacial charge transfer and separation through heterojunction formation, leading to enhanced photocatalytic efficiency[25–30] The intimate contact between CD and g-C_3N_4 promotes efficient electron transfer across the interface, facilitating rapid redox reactions and improving overall catalytic activity.[31] Additionally, the presence of CD can alter the band structure of g-C_3N_4, leading to a red shift in the light absorption spectrum and enabling utilization of a broader range of solar radiation for photocatalysis.[32]

This study delves into enhancing the photocatalytic efficacy of g-C_3N_4 by sulfur doping and incorporating CD into its structure. Through systematic investigation, we aim to elucidate the mechanisms underlying the superior performance of g-C_3N_4 as a photocatalyst, particularly focusing on sulfur doping effects. Our efforts contribute to advancing the understanding of these materials for environmental remediation purposes. Moreover, we explore the potential of SCN/CD nanocomposites in degrading CECs such as BPA and TC, crucial for sustainable environmental cleanup initiatives. This research underscores the significance of tailored modifications in g-C_3N_4 to optimize its photocatalytic activity, paving the way for efficient degradation of CECs and promoting environmentally friendly remediation strategies.

2. Experimental section

2.1. Materials and method

The chemical reagents, namely thiourea (CH_4N_2S: ≥99.0%), urea ($CO(NH_2)_2$: 99.0%), citric acid ($C_6H_8O_7$: ≥99.5%), bisphenol A ($C_{15}H_{16}O_2$: 99.0%), tetracycline ($C_{22}H_{24}N_2O_8$: ≥95.0%), and ethanol (C_2H_6O: 98.0%) were purchased from Sigma-Aldrich, with excellent analytical quality. They were used just as received, with no further refinement. Every solution was prepared using deionized water as the medium.

2.2. Synthesis of CD

A hydrothermal process was employed to create CD. Initially, ultrasonication was used for two hours to dissolve 1.0 g of citric acid and 2.0 g of urea in deionized water. After that, the mixture was placed inside a 150 mL Teflon-lined stainless-steel autoclave and heated to 200 °C for 8 hours to undergo hydrothermal treatment. To get rid of big particles, the black solution was centrifuged for 30 minutes after it cooled to normal temperature and ultimately, the supernatant was gathered.[33]

2.3. Synthesis of SCN/CD

The CD/SCN photocatalyst was synthesized using a thermo-polymerization method. In the standard procedure, 2.0 g of thiourea was mixed with a specific volume of CD solution in 10 mL of deionized water. Following the evaporation of the solution at 70 °C, the resulting powder underwent heating to 550 °C for 3 hours, with a gradual increase in temperature at a rate of 2.8 °C per minute. The resultant CD/SCN powder was obtained through meticulous grinding and filtration. Different SCN/CD samples were prepared with varying CD contents (1%, 2%, 3%, and 4% by weight), designated as SCN/CD1, SCN/CD2, SCN/CD3, and SCN/CD4, respectively. Sulphur atoms entered the g-C_3N_4 network *in situ* during the thermal polycondensation process when SCN samples were synthesised without the addition of CD solution.[34] The schematic illustration of the synthesis procedure is shown in Fig. 1.

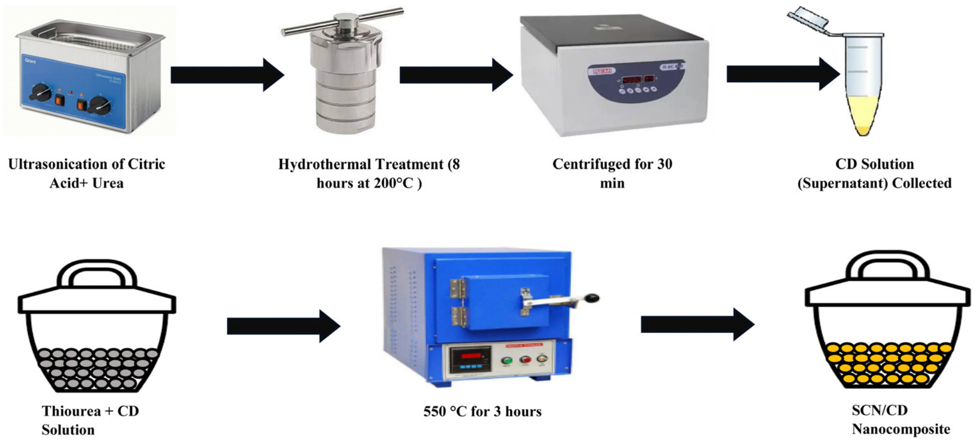

Fig. 1 Schematic representation of synthesis process of CD and SCN/CD.

3. Characterizations

3.1. X-ray diffraction (XRD)

XRD analysis was conducted within the angular range of 5° to 60°, offering valuable information on the structural properties of the CD, SCN and their combined nanocomposite under investigation. In Fig. 2, CD exhibited a broad hump centred at 21.8° on the (002) plane, indicating the presence of an amorphous carbon phase. Pure SCN displayed a minor peak at 12.8° implying the presence of regularly recurring units of the heptazine structure on the (100) plane. The significant peak at 27.5° indicated the layered arrangement of π-conjugated aromatic structures of g-C_3N_4 layers on the (002) plane.[35] Analysis of the SCN/CD nanocomposite revealed peaks resembling those of pure SCN, with no discernible CD peaks. A slight shift towards lower angles and a decrease in peak height were observed, attributed to CD amorphous nature, indicating some alteration due to lattice distance augmentation. Notably, XRD patterns remained consistent across varying CD concentrations, suggesting minimal influence on the lattice structure of SCN. This observation underscores the stability of SCN's lattice structure despite changes in CD concentration, as evidenced by uniform XRD profiles across the investigated CD concentration range.[36]

3.2. Fourier transform infrared spectroscopy (FTIR)

The surface functionality of prepared nanocomposites was analysed using FTIR as shown in Fig. 3. In SCN spectra a broad peak in the region of 3050–3400 cm^{-1} was observed and identified as the N–H stretching vibration in terminal amino groups (–NH_2 or =NH groups). The peaks at 1636 cm^{-1} and 1538 cm^{-1} indicated the C=N stretching vibration of the triazine unit, while peaks at 1400 cm^{-1}, 1315 cm^{-1}, and 1206 cm^{-1} corresponded to the C–N stretching. Additionally, the out-of-plane stretching of the tri-*s*-triazine unit was identified at 815 cm^{-1}.[37] Vibrations associated with the S-related group were minimal in doped g-C_3N_4, possibly due to the low sulfur content and overlapping with C–N vibration peaks. In the FTIR spectrum of CD, the broad bump at 3407 cm^{-1} were attributed to O–H stretching, with peaks at 2973 cm^{-1} and 1619 cm^{-1} associated with –C–H stretching and C=C stretching, respectively. Peaks at 1369 cm^{-1} and 1050 cm^{-1} corresponded to C–N stretching vibrations.[38] Notably, in the SCN/CD spectrum, significant changes in the characteristic bands of SCN were observed, indicating potential interfacial interactions between CD and SCN. The FTIR spectra for a series of nanocomposites with varying concentrations of CD (1%, 2%, 3%, 4%) exhibited no discernible changes, indicating that the spectra remained consistent across different CD concentrations. This implies that the FTIR characteristics of the nanocomposites were not substantially changed by the addition of CD.

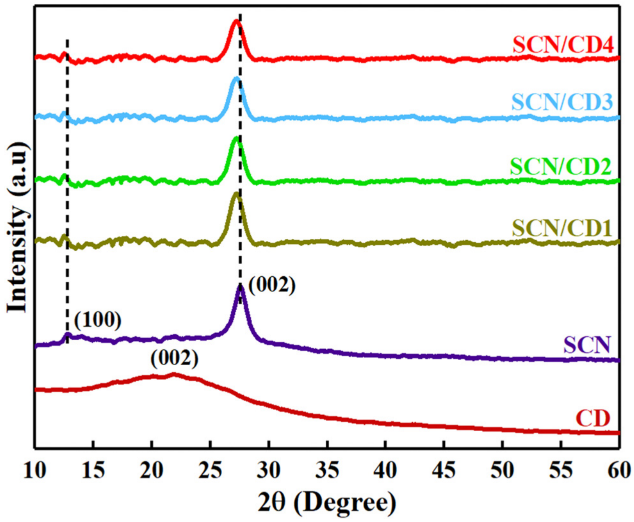

Fig. 2 XRD patterns of CD, SCN and SCN/CD nanocomposites.

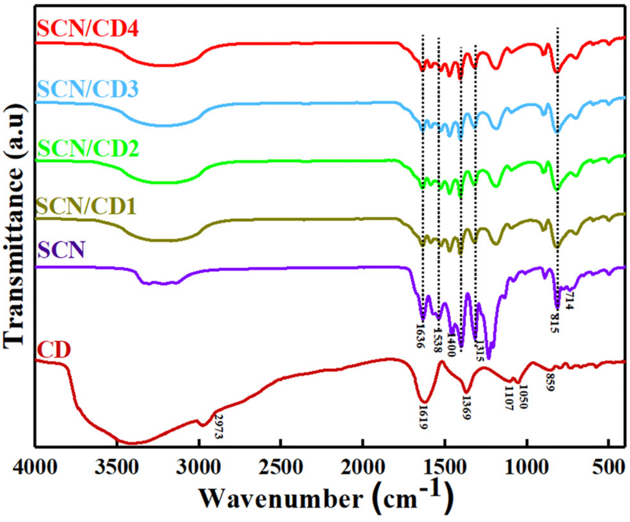

Fig. 3 FTIR patterns of CD, SCN and SCN/CD nanocomposites.

3.3. X-ray photoelectron spectroscopy (XPS)

XPS analysis of both the SCN and SCN/CD samples confirmed the presence of carbon (C), nitrogen (N), oxygen (O), and sulfur (S) components as shown in Fig. 4. Notably, the relative ratio of oxygen was higher in the SCN/CD3 sample, possibly due to absorbed water and oxygen by the CD. The C 1s transition displayed peaks at 287.2 eV, indicating sp^2 N–C=N bonds, and at 284.3 eV, associated with aromatic C atoms in the *s*-triazine ring. In the N 1s region, peaks were detected at 397.6, 398.5, 400.3, and 403.3 eV, representing various nitrogen-containing groups such as sp^2 hybridization of localized nitrogen, tertiary N–$(C)_3$ groups, amino groups with hydrogen, and pi excitations. Peaks observed in the O 1s region at 530.6 eV and 532.6 eV likely stemmed from O–C/O–H and O–C components, potentially due to absorbed water and oxygen. Additionally, a distinct peak at 164 eV indicated the presence of a C–S bond, suggesting sulfur incorporation into the lattice structure, possibly through substitution with lattice nitrogen.[32,39]

3.4. Ultraviolet-visible diffused reflectance spectroscopy (UV-DRS)

The optical absorption characteristics of the samples were probed using UV-visible diffuse reflectance spectroscopy. The

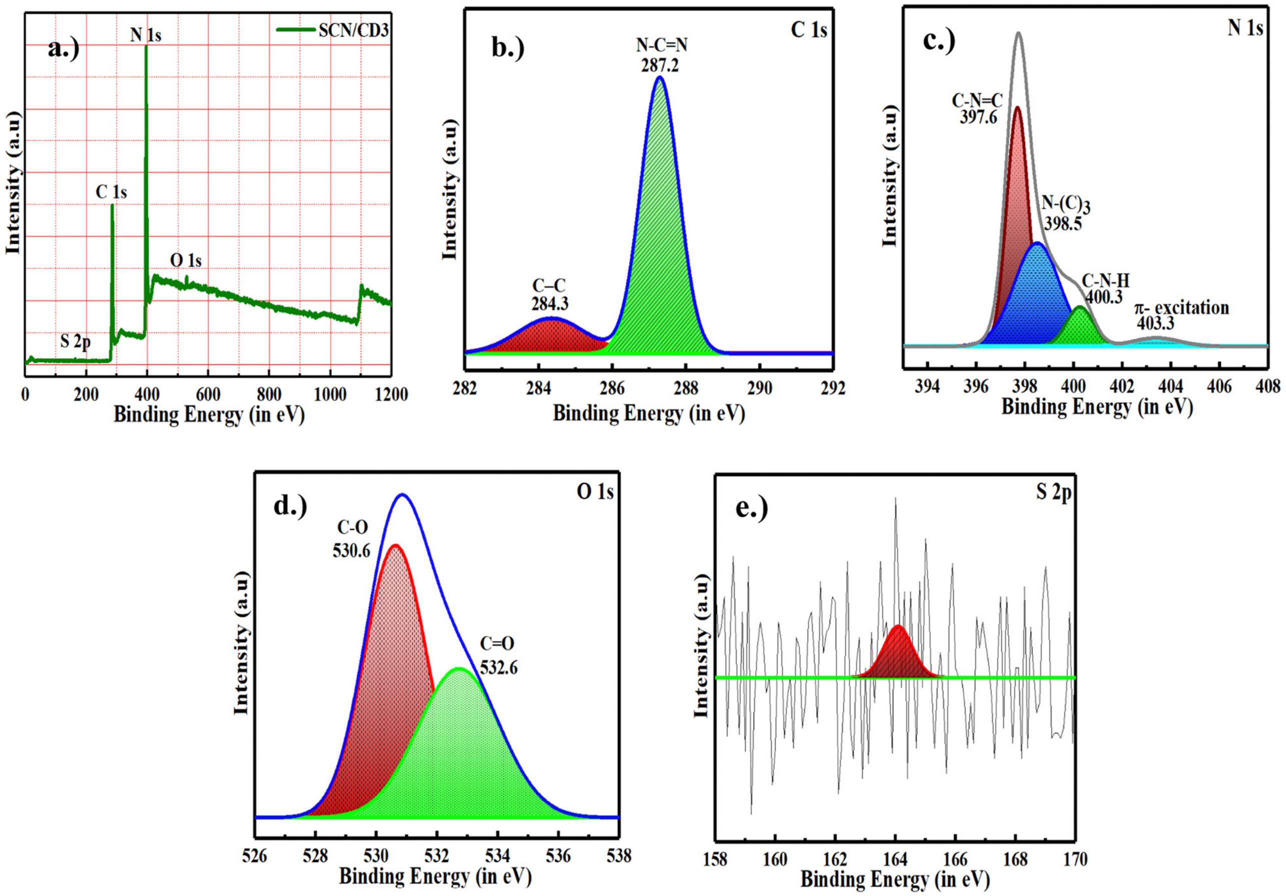

Fig. 4 (a) XPS spectra of SCN/CD3 nanocomposite. High resolution spectra of (b) carbon, (c) nitrogen (d) oxygen and (e) sulfur.

absorption onset for pristine was found at approximately 470 nm, while for both sulfur-doped carbon nitride (SCN) and SCN/CD nanocomposites, it shifted to around 500 nm as shown in Fig. 5(a). Interestingly, the incorporation of cyclodextrin (CD) into SCN led to a redshift in the absorption edge of the SCN/CD nanocomposite, along with an enhancement in light absorption within the visible spectrum. The semiconductor bandgap was determined using the Tauc plot method, where the absorption coefficient (α) was plotted against the photon energy ($h\nu$). Fig. 5(b) analysis revealed a decrease in the bandgap from

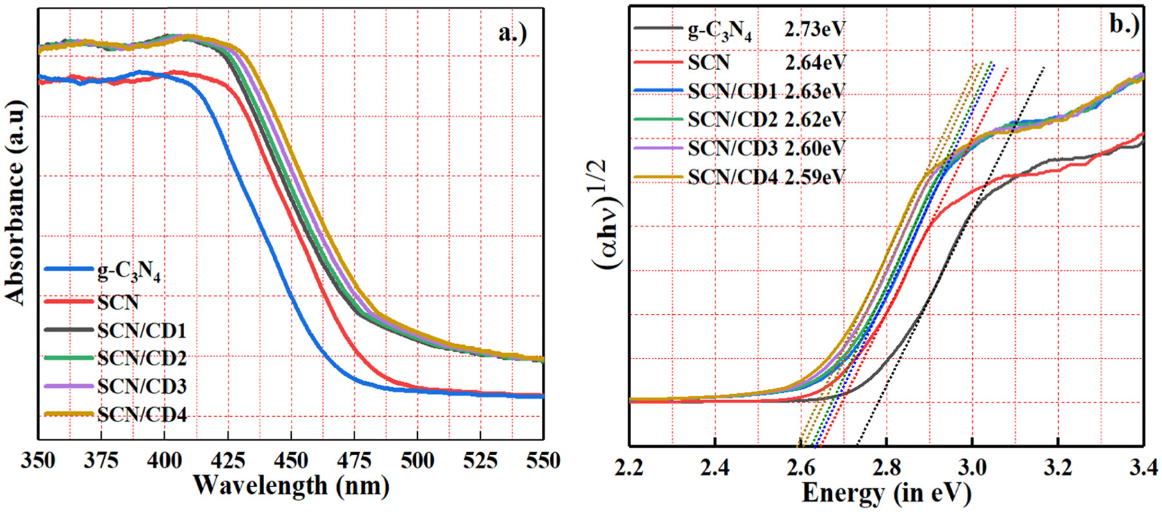

Fig. 5 (a) UV-vis diffuse reflectance of g-C_3N_4, SCN, SCN/CD1, SCN/CD2, SCN/CD3 and SCN/CD4 (b) Tauc plot representing the bandgap energies of g-C_3N_4, SCN, SCN/CD1, SCN/CD2, SCN/CD3 and SCN/CD4.

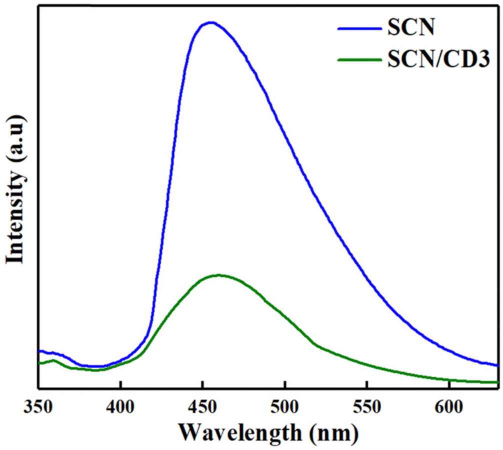

Fig. 6 PL spectra of synthesised nanocomposite SCN and SCN/CD3.

2.73 eV for g-C_3N_4 to 2.64 eV for SCN, indicating that SCN has a superior ability to harness visible light compared to pristine g-C_3N_4. Moreover, with the introduction of CD into SCN, the bandgap decreased further with increasing CD concentration, suggesting that CD incorporation marginally affects the nanocomposite's bandgap, potentially indicating CD's primary localization on the SCN surface.[40] Despite this, the narrowed bandgap shows promise for improving visible light absorption, facilitating the generation of photoinduced carriers.

3.5. Photoluminescence (PL) spectroscopy

PL spectroscopy was employed to examine the dynamics of electron–hole pair separation and recombination in SCN and SCN/CD3. With an excitation wavelength of 325 nm, SCN exhibited a distinct emission peak at approximately 455 nm, whereas SCN/CD3 displayed a slight red shift, manifesting a peak around 460 nm as shown in Fig. 6. Notably, the emission intensity of SCN/CD3 was notably lower than that of pristine SCN, indicating a significant suppression of electron–hole pair recombination within the composite photocatalysts.[41] This suppression suggests efficient charge separation, facilitated by the combination of CDs with SCN, which accelerates electron transfer while hindering the recombination process, ultimately enhancing photocatalytic performance.

3.6. Electrochemical impedance spectroscopy (EIS)

The Nyquist plots generated from EIS data were utilized to assess the interfacial charge transfer characteristics of the synthesized photocatalysts. Typically, the arc radius observed in Nyquist plots corresponds to the reaction rate occurring at the working electrode. A smaller arc radius indicates a lower resistance electrode, suggesting efficient separation of electron–hole pairs and an adequate supply of electrons for the photodegradation reaction. In Fig. 7, it is observed that the SCN exhibited a larger arc radius compared to SCN/CD3. The observation implies that SCN/CD3 possesses the lowest resistance for charge transfer, indicating more effective separation of photoinduced charges.[42,43] Such enhanced charge separation is beneficial for improving photocatalytic performance, as it facilitates efficient utilization of photogenerated charge carriers.

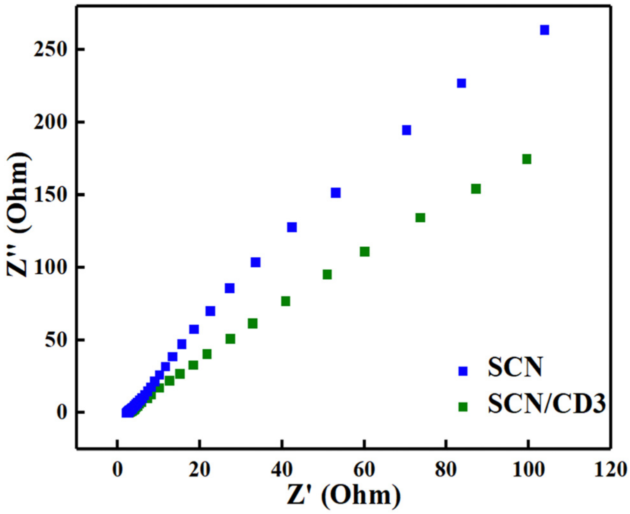

Fig. 7 EIS Nyquist plots of SCN and SCN/CD3.

3.7. Scanning electron microscope (SEM)

The morphology, structure, and elemental distribution of a nanocomposite were investigated using SEM. Fig. 8 depicts SEM images of both pure SCN and SCN/CD nanocomposite. The surface of SCN comprises flat and stratified nanosheets arranged in layers. In contrast, in the SCN/CD nanocomposite, the SEM images reveal the presence of small spherical CD particles dispersed on the surface of the SCN layered structure. Importantly, these CD particles are not merely adhering to the surface but are embedded within the SCN surface itself, effectively acting as intrinsic surface modifiers. This embedded configuration ensures intimate contact between the CD particles and the SCN material, enhancing their catalytic performance and efficiency in the photocatalytic degradation process. Also, the sheet-like morphology providing large surface area further facilitates the adsorption of organic molecules, thereby increasing the proportion of catalytically active sites on the surface. This enhancement contributes to the photocatalytic degradation process.

3.8. Energy dispersive X-ray spectroscopy (EDX)

The EDX analysis of the SCN/CD nanocomposite reveals significant insights into its elemental composition. As shown in Fig. 9(a), distinct peaks corresponding to carbon (C), nitrogen (N), oxygen (O), and sulfur (S) elements were observed at specific energy levels: the peak for carbon appears at 0.3 keV, nitrogen at 0.5 keV, oxygen at 0.8 keV, and sulfur at 2.2 keV. Quantitative analysis shows that carbon and nitrogen dominate the composition, with weight percentages of 40.5% and 56.9% respectively, suggesting their substantial incorporation into the nanocomposite structure. Oxygen contributes 2.3% by weight, while sulfur comprises a minor fraction at 0.3%. The presence

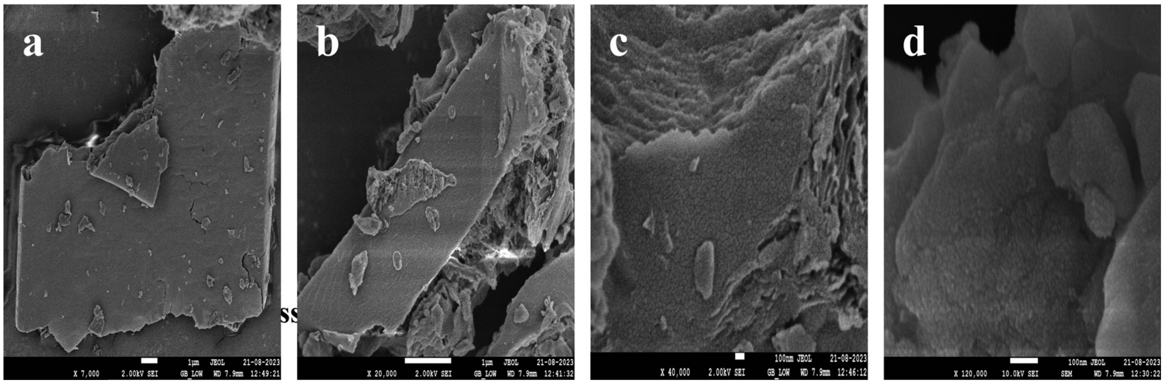

Fig. 8 SEM images of (a) SCN (b) SCN at higher magnification (c) SCN/CD (d) SCN/CD at higher magnification.

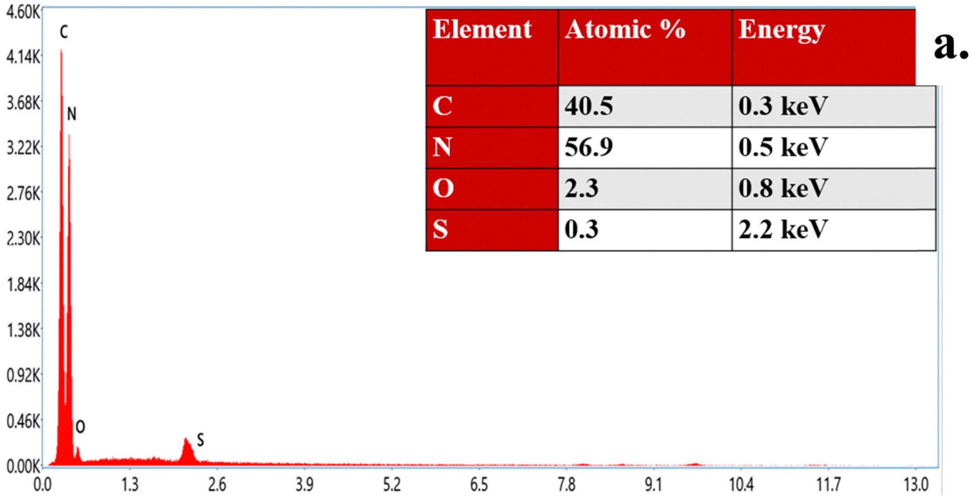

Element	Atomic %	Energy
C	40.5	0.3 keV
N	56.9	0.5 keV
O	2.3	0.8 keV
S	0.3	2.2 keV

Fig. 9 (a) EDX pattern of SCN/CD.

of small amount of sulfur confirms its doping into the nanocomposite. These findings not only highlight the relative abundance of each element but also shed light on the chemical composition and potential functional groups present in the nanocomposite.

4. Results and discussion

4.1. Evaluation of catalytic performance

The photodegradation experiment was conducted within a closed wooden box, exposed to ambient air conditions, utilizing two 250-watt tungsten lamps as a visible light source. The 50 ppm solutions of organic pollutant containing TC and BPA were individually prepared in separate 1-liter volumetric flasks filled with distilled water. In the experimental setup, 50 mg of catalyst was dispersed into 100 mL of the solution containing the organic pollutants.[44,45] To establish adsorption–desorption equilibrium, the solution was gently stirred and allowed to incubate in darkness for thirty minutes before exposure to visible light. Throughout the irradiation process, 5 mL samples of the suspension were collected at 15-minute intervals and subsequently subjected to centrifugation to isolate the photocatalyst for analysis at specific irradiation times. The photodegradation efficiency (%) was determined using UV-visible spectrophotometry, measuring the maximum absorbance ($\lambda_{\max}$) of both compounds as shown in Fig. 10(a)–(d). We used the following equation to obtain the (%) photodegradation efficiency:[46]

$$(\%)\ \text{photodegradation efficiency} = \{(C_o - C_t)/C_o\} \times 100 \tag{1}$$

Assessing the photocatalytic prowess of our composite materials under visible light exposure, we employed BPA and TC as model pollutants. Both pollutants exhibited poor natural degradation properties. Among the composite materials as shown in Fig. 11(a)–(d), SCN/CD3 demonstrated the highest photocatalytic degradation rate, achieving remarkable removal rates of 92.5% for BPA and 90.7% for TC after just 60 minutes of reaction time. SCN alone also exhibited relatively effective degradation efficiencies of 68.5% for BPA and 60% for TC, attributed to its ability to absorb visible

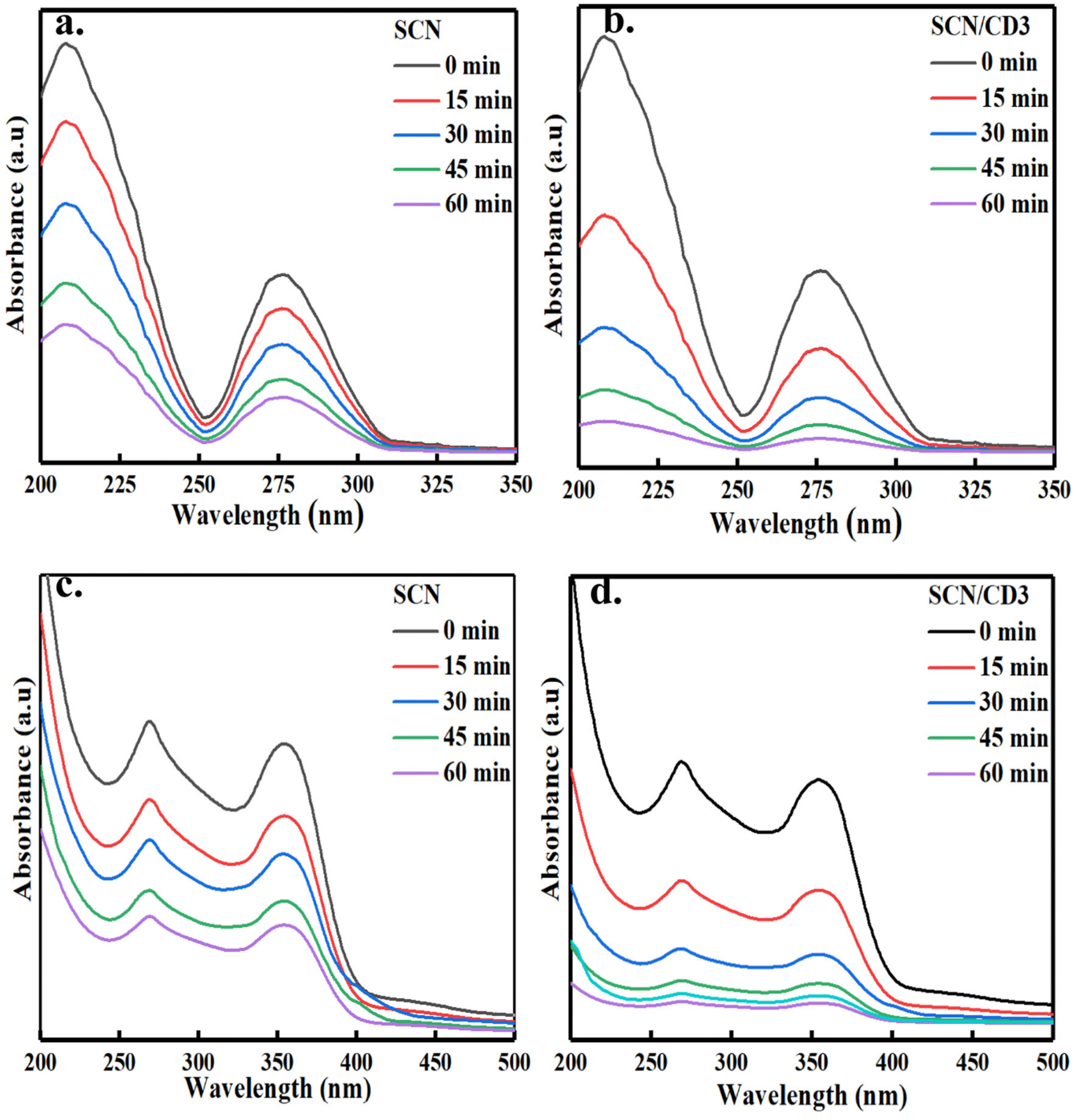

Fig. 10 UV-visible absorbance spectra of visible light degradation of BPA in presence of (a) SCN (b) SCN/CD3. UV-visible absorbance spectra of visible light degradation of TC in presence of (c) SCN (d) SCN/CD3.

light.The incorporation of CD into the composite narrowed the band gap, resulting in enhanced photosensitivity and broader absorption bands in the visible and near-infrared (NIR) light regions compared to pure SCN. This suggests that the introduction of CD acts as an electron reservoir, facilitating electron excitation in both CD and g-C_3N_4, thus generating more electron–hole pairs for pollutant degradation. However, an excessive concentration of CD may suppress electron–hole pair generation, underscoring the need to optimize CD concentration for optimal results. The photodegradation kinetics of BPA and TC followed pseudo-first-order kinetics. The calculated rate constants (k values) for various composite combinations against BPA and TC provide insights into their degradation efficiency as shown in Table 1. Additionally, we reviewed and compared various studies exploring the degradation of BPA and TC using different nanomaterials, as summarized in Table 2.

4.2. Recycalibity and photostability

The preservation of photocatalytic efficacy stands as a pivotal criterion in the evaluation of the durability and recyclability of the synthesized SCN/CD3 nanocomposites as photocatalysts. To gauge the potential for reuse, several degradation cycles were conducted with the SCN/CD3 nanocomposite. Following each cycle, the nanocomposite underwent centrifugation to extract it from the solution, followed by rinsing with distilled water and subsequent drying at 60 °C for two hours.[53,54] Notably, even after undergoing five degradation cycles, the nanocomposite sustained a degradation efficiency of over 90% for BPA and maintained an efficiency of 88% for TC, as

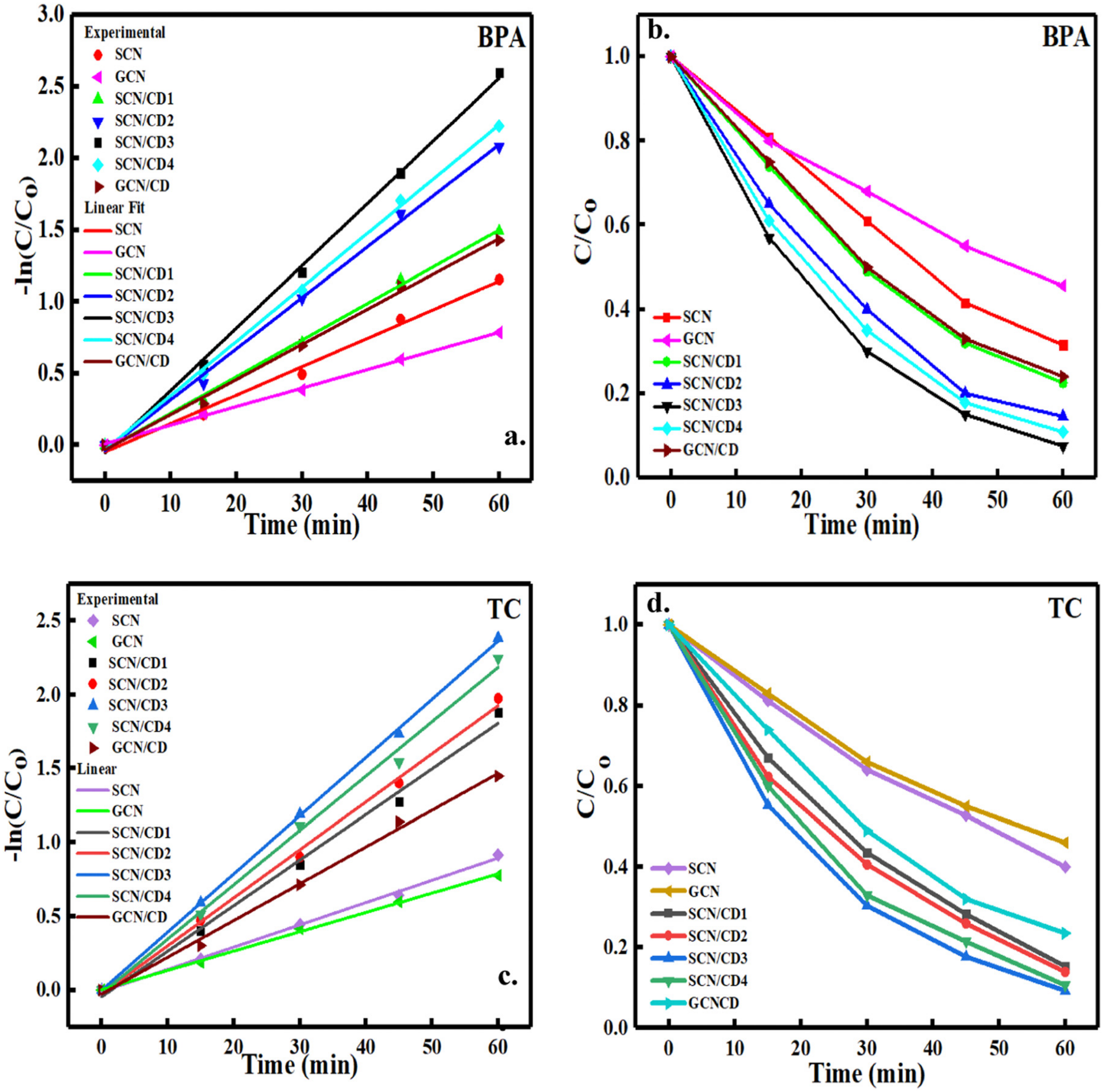

Fig. 11 (a) Photodegradation performance of BPA (b) first-order plots of BPA (c) photodegradation performance of TC (d) first-order plots of TC over the prepared nano catalysts under visible light using two 250 W Tungsten Lamp.

illustrated in Fig. 12(a). Additionally, as shown in Fig. 12(b), the XRD pattern analysis of the nanocomposite before and after degradation experiments revealed identical diffraction peaks, indicative of the robustness of the nanocomposite's structure and its enduring photocatalytic activity across multiple degradation cycles.

4.3. Radical trapping

The primary reactive species involved were determined through a free radical trapping experiment. Specifically, EDTA, isopropyl (IPA), and benzoquinone (BQ) were utilized as scavengers for holes, hydroxyl radicals, and superoxide radicals, respectively. A decrease in degradation efficiency within the reaction system typically suggests the prevalence of major active species. Each scavenger was incorporated into the reaction mixture at a concentration of 0.1 mM.[55] Comparative analysis with the absence of scavengers revealed that all scavengers exhibited a partial suppression of photocatalytic efficiency, as depicted in Fig. 13. While IPA had a marginal effect on restraining the photodegradation efficiency of BPA and TC, the most significant reduction in the rate of photodegradation was observed in the batch treated with BQ and EDTA. This indicates that superoxide and hole radicals played pivotal roles in the photocatalytic degradation process.

4.4. Possible mechanism for degradation of BPA and TC

The degradation mechanism of BPA and TC over SCN/CD3 composite under visible light irradiation is depicted in Scheme 1, offering a nuanced understanding of the process. The determination of relative band position of SCN and SCN/CD3 was achieved through the measurement of flat band potential from Mott–Schottky plot, indicating both SCN and SCN/CD3 as an n-type semiconductor. With conduction band

Table 1 Insights into the photodegradation percentage and rate constants by different nanocomposite against BPA and TC

S. no.	Photocatalyst	Photodegradation efficiency (%)	Rate constant (k in min^{-1})	R^2
Performance against bisphenol A (BPA)				
1.	SCN	68.5	0.0198	0.995
2.	SCN/CD1	77.5	0.0255	0.996
3.	SCN/CD2	87.5	0.0355	0.997
4.	SCN/CD3	92.5	0.0435	0.998
5.	SCN/CD4	89.2	0.0378	0.997
6.	g-C_3N_4	54.4	0.0130	0.997
7.	g-C_3N_4/CD	76.0	0.0245	0.995
Performance against tetracycline (TC)				
1.	SCN	60	0.0151	0.997
2.	SCN/CD1	84.7	0.0309	0.996
3.	SCN/CD2	86.1	0.0325	0.998
4.	SCN/CD3	90.7	0.0394	0.999
5.	SCN/CD4	89.4	0.0368	0.995
6.	g-C_3N_4	54.0	0.0131	0.997
7.	g-C_3N_4/CD	76.5	0.0249	0.994

(CB) position of −1.03 eV *vs.* Normal hydrogen electrode (NHE) for SCN as shown in Fig. 14. By considering the optical band energy obtained from UV-DRS spectra, the band gap energy (E_g) of SCN is calculated to be 2.64 eV. Using this value, along with the measured flat band potential, the valence band (VB) energy is calculated to be 1.61 eV *vs.* NHE. Similarly, for the SCN/CD3 composite, the Mott–Schottky analysis revealed the flat band potential of SCN/CD3 to be −1.57 eV, representing the energy of the conduction band. With the band gap from UV-DRS calculated as 2.60 eV, the energy of the valence band for SCN/CD3 was estimated to be 1.03 eV *vs.* NHE. Furthermore, the potential energy diagram *vs.* NHE for the composite illustrates the staggered band edge potentials between SCN and CD, forming heterojunctions at the interfaces.[56] Moreover, the CD serve a dual role, acting as both a photosensitizer and an electron mediator, thus expanding the photon absorption range effectively. Also, the incorporation of CD triggers alterations in the electron density distribution within the SCN/CD composite, thereby curbing the recombination of electron–hole pairs (e^-/h^+). Moreover, the ultra-thin structure of SCN/CD promotes swift electron transfer from the interior to the surface of the photocatalyst. Upon exposure to visible light, electrons (e^-) within the SCN/CD3 composite are excited from the VB to the CB, leading to the formation of holes (h^+) in the VB. Notably, the accumulated electrons within SCN/CD readily react with oxygen in the solution, yielding $O_2^{\bullet-}$ (0.13 eV *vs.* NHE). However, the system lacks the capacity to oxidize water for $OH^\bullet$

Table 2 The degradation efficiency of TC and BPA under various light irradiation compared with previous reports

S. no.	Photocatalyst	Organic pollutant	Degradation percentage (%)	Time (in min)	Light	Ref.
1.	CDs/g-C_3N_4/MoO_3	Tetracycline	81	90	Visible	47
2.	N-CQDs/g-C_3N_4/PDS	Tetracycline	90	60	Visible	48
3.	CDs/H-CN	Tetracycline	86	120	Visible	49
4.	CDs/g-C_3N_4	Bisphenol A	90	180	Visible	50
5.	RGO/g-C_3N_4	Bisphenol A	90	90	Visible	51
6.	In_2O_3/OGCN	Bisphenol A	91	180	Visible	52
7.	SCN/CD	Bisphenol A	92.5	60	Visible	This work
8.	SCN/CD	Tetracycline	90.7	60	Visible	This work

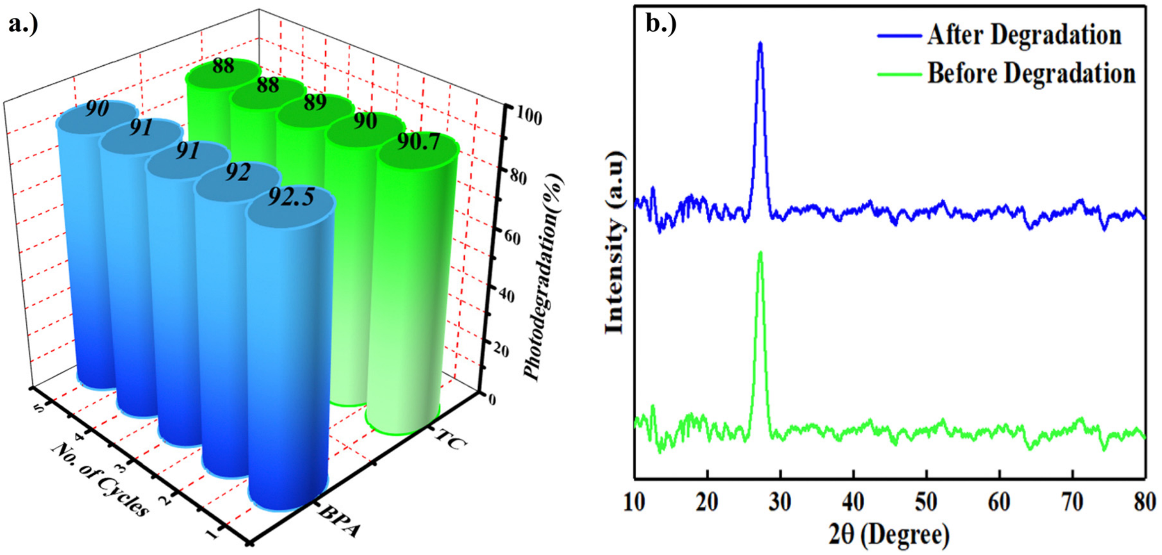

Fig. 12 (a) Five photocatalytic degradation cycles of BPA and TC using SCN/CD3 under visible light irradiation (b) the XRD patterns of the as-prepared GZP1 before and after five cycles.

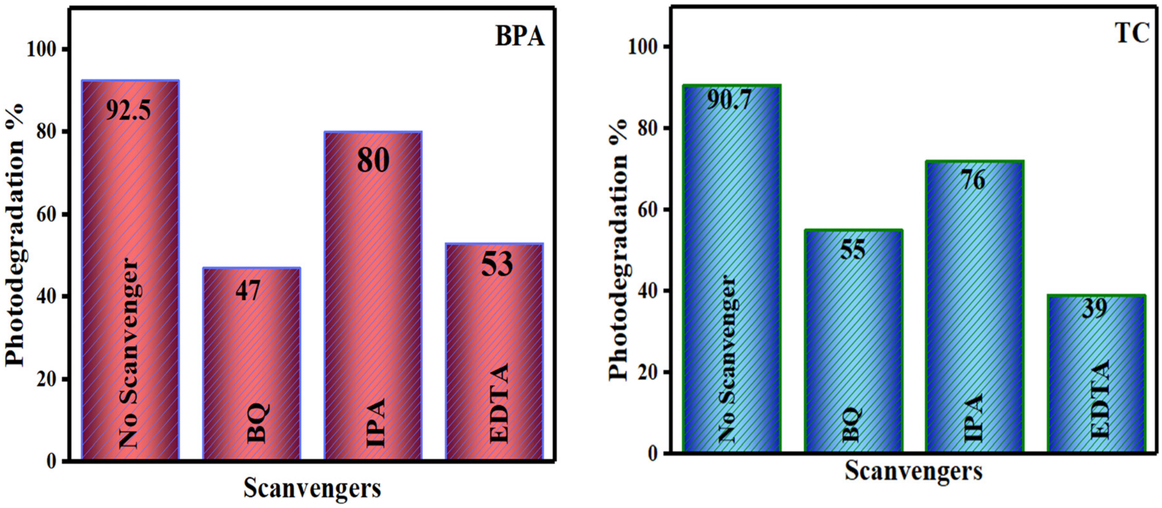

Fig. 13 Influence of radical scavengers for photodegradation of BPA and TC on SCN/CD3 under visible light irradiation.

production (2.68 *vs.* NHE). Consequently, $OH^•$ generation occurs through the homolytic scission of H_2O_2, originating from the reduction of $O_2^{•-}$. Additionally, the holes (h^+) present in SCN/CD3 actively participate in the degradation of TC and BPA. The ultrathin structure of SCN/CD provides abundant active sites, facilitating the facile adsorption of both BPA and TC onto the photocatalyst's surface. Subsequently, these organic pollutants undergo degradation *via* the action of reactive species, notably $O_2^{•-}$and h^+, culminating in their breakdown and complete mineralization.[57–60] This elucidated mechanism provides a comprehensive insight into the intricate degradation processes of BPA and TC over the SCN/CD3 composite, emphasizing the pivotal roles played by CD and SCN in driving pollutant degradation under visible light irradiation.

4.5. Mechanistic degradation of BPA and TC by prepared catalyst

Liquid chromatography-mass spectrometry (LC-MS) analysis was conducted to gain insight into the intermediates formed during the degradation process and the potential mechanistic pathway of BPA and TC in the presence of SCN/CD composites. Over a span of 60 minutes, a substantial detoxification of 92.5% for BPA and 90.7% for TC was achieved, indicating the effectiveness of the photocatalytic process. LC-MS analysis unveiled many intermediate products arising from the degradation of TC and BPA. It was observed that BPA and TC, along with their generated fragments, underwent reactions with reactive species, ultimately leading to the generation of water and carbon dioxide. For BPA, a gradual conversion into lower weight molecules such as aromatic intermediates, benzoquinones, and carboxylic acids was evident. The mechanisms underlying this degradation process involve various reactions including substitution on the aromatic ring, hydroxylation of the aromatic ring, decarboxylation, dehalogenation, bond cleavage, and ring-opening. The LC-MS analysis facilitated the identification of several intermediate products, characterized by specific mass-to-charge ratio (*m*/*z*) values. For instance, during the

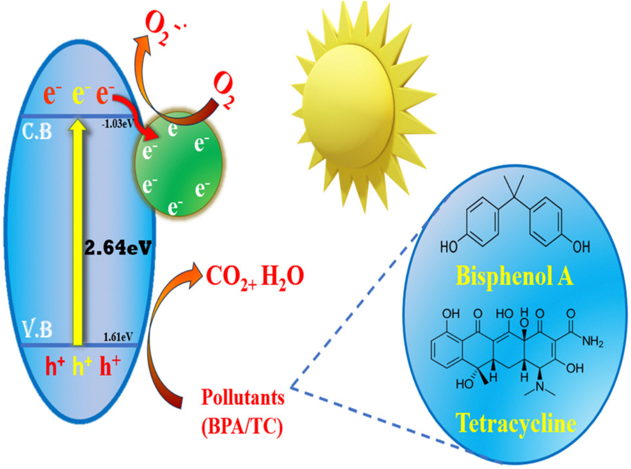

Scheme 1 Schematic diagram for probable mechanism of photocatalysis.

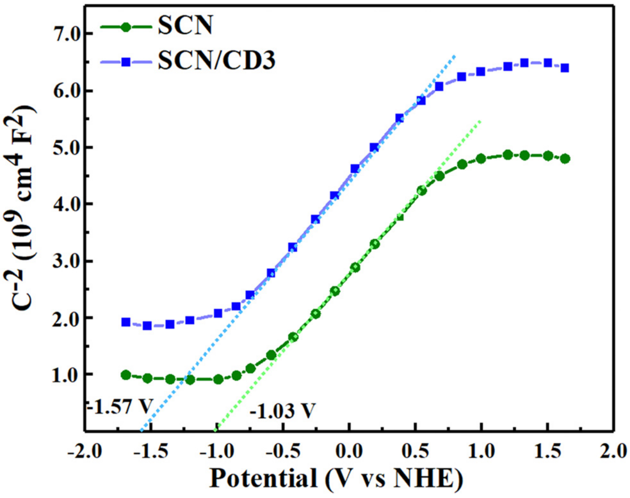

Fig. 14 Mott Schottky curve of SCN and SCN/CD3.

decomposition of BPA by the prepared photocatalyst, intermediate compounds with *m*/*z* values of 208, 197, 104, 108, 152, 122, and 135 were detected.[61] Similarly, active species targeted double bonds, aromatic rings, amino groups, leading to ring-opening reactions, loss of functional groups, or rupture of primary carbon bonds, thereby generating many intermediates in the case of TC. The intermediate compounds formed during the decomposition of TC exhibited *m*/*z* values of 445, 272, 238, 433, 301, 149, 210, 438, 139, and 103.[62] This comprehensive LC-MS analysis provides valuable insights into the intermediates formed during the degradation process, shedding light on the potential degradation pathways followed by BPA and TC under photocatalytic conditions. Information regarding the proposed degradation pathway and intermediates is provided in S1 (ESI†), offering a detailed elucidation of the mechanisms underlying the photocatalytic degradation of BPA and TC.

5. Conclusion

The sulfur modification of g-C_3N_4 coupled with the integration of CD into the nanocomposite yields a significant enhancement in visible light activity and efficiency for photocatalytic degradation of CECs like BPA and TC. Within the SCN material, the presence of CD serves as electron reservoirs, effectively mitigating electron–hole recombination and thereby augmenting pollutant degradation. Particularly noteworthy is the exceptional efficiency demonstrated by the SCN/CD3 photocatalyst, achieving BPA degradation rates of up to 92.6% and TC degradation rates of up to 90.7% within a brief 60-minute irradiation period under visible light. Remarkably, the catalyst maintains high degradation efficiency over five cycles, with superoxide radicals ($O_2^{\bullet -}$) and holes (h^+) identified as the primary reactive species responsible for pollutant degradation. Broadening the scope of pollutant targets beyond BPA and TC to encompass a wider range of CECs prevalent in various environmental matrices will increase the applicability and relevance of SCN/CD composites in environmental remediation efforts. These endeavours hold significant promise for making substantial contributions to sustainable pollution mitigation strategies.

Author contributions

Ankoor Sura: conceptualization, formal analysis, investigation, writing – original draft preparation, methodology, visualization. Arjun Singh, Sudha Narwal, Priya Malik and Amanvir Singh: data curation, formal analysis. visualization and investigation. Sonia Nain and Surender Duhan: project administration, conceptualization, formal analysis, resources, investigation, supervision, reviewing and editing.

Conflicts of interest

The authors declare no competing financial and/or non-financial interests.

Acknowledgements

One of the authors, Ankoor Sura is thankful to CSIR (New Delhi), for providing financial support under the JRF scheme. The authors would also like to acknowledge SAIF-AIIMS (New Delhi), Central Research Facility, IIT Delhi, and Central Instrumentation Laboratory Deenbandhu Chhotu Ram University of Science and Technology, Murthal for providing instrumentation facilities.

References

1 D. Yadav, S. Rangabhashiyam, P. Verma, P. Singh, P. Devi and P. Kumar, *et al.*, Environmental and health impacts of contaminants of emerging concerns: Recent treatment challenges and approaches, *Chemosphere*, 2021, **272**, 129492.
2 T. K. Kasonga, M. A. A. Coetzee, I. Kamika, V. M. Ngole-Jeme and M. N. Benteke Momba, Endocrine-disruptive chemicals as contaminants of emerging concern in wastewater and surface water: A review, *J. Environ. Manage.*, 2021, **277**, 111485.
3 M. Antoniadou, P. P. Falara and V. Likodimos, Photocatalytic degradation of pharmaceuticals and organic contaminants of emerging concern using nanotubular structures, *Curr. Opin. Green Sustainable Chem.*, 2021, **29**, 100470.
4 H. Pokkiladathu, S. Farissi, A. Sakkarai and M. Muthuchamy, Degradation of bisphenol A: a contaminant of emerging concern, using catalytic ozonation by activated carbon impregnated nanocomposite-bimetallic catalyst, *Environ. Sci. Pollut. Res.*, 2022, **29**(48), 72417–72430.
5 M. Salimi, A. Esrafili, M. Gholami, A. Jonidi Jafari, R. Rezaei Kalantary and M. Farzadkia, *et al.*, Contaminants of emerging concern: a review of new approach in AOP technologies, *Environ. Monit. Assess.*, 2017, **189**(8), 414.
6 M. Antoniadou, P. P. Falara and V. Likodimos, Photocatalytic degradation of pharmaceuticals and organic contaminants of emerging concern using nanotubular structures, *Curr. Opin. Green Sustainable Chem.*, 2021, **29**, 100470.
7 A. Balakrishnan, M. Chinthala, R. K. Polagani and D. V. N. Vo, Removal of tetracycline from wastewater using g-C_3N_4 based photocatalysts: A review, *Environ. Res.*, 2023, **216**, 114660.
8 B. L. Phoon, T. C. K. Yang, B. F. Leo, C. W. Lai, S. W. Phang and J. C. Juan, Mesoporous semi-ionic F-doped g-C_3N_4 as efficient photocatalyst for tetracycline removal under visible light, *Environ. Technol. Innovation*, 2023, **32**, 103303.
9 J. N. Hahladakis, E. Iacovidou and S. Gerassimidou, An overview of the occurrence, fate, and human risks of the bisphenol-A present in plastic materials, components, and products, *Integr. Environ. Assess. Manage.*, 2023, **19**(1), 45–62.
10 Q. Yi, Y. Gao, H. Zhang, H. Zhang, Y. Zhang and M. Yang, Establishment of a pretreatment method for tetracycline production wastewater using enhanced hydrolysis, *Chem. Eng. J.*, 2016, **300**, 139–145.

11 K. Li, A. Yediler, M. Yang, S. Schulte-Hostede and M. H. Wong, Ozonation of oxytetracycline and toxicological assessment of its oxidation by-products, *Chemosphere*, 2008, **72**(3), 473–478.

12 T. Yamamoto, A. Yasuhara, H. Shiraishi and O. Nakasugi, Bisphenol A in hazardous waste landfill leachates, *Chemosphere*, 2001, **42**(4), 415–418.

13 Y. Q. Huang, C. K. C. Wong, J. S. Zheng, H. Bouwman, R. Barra and B. Wahlström, *et al.*, Bisphenol A (BPA) in China: A review of sources, environmental levels, and potential human health impacts, *Environ. Int.*, 2012, **42**, 91–99.

14 A. Singh, V. Kaushik, V. Kumari, A. Goswami and S. Nain, Impact of Variable Metal Oxide Loadings on Photocatalytic and Antibacterial Behaviour of CNT-NiO Nanocomposites, *Bionanoscience*, 2023, **13**(4), 1885–1895.

15 S. Patnaik, D. P. Sahoo and K. Parida, Recent advances in anion doped g-C_3N_4 photocatalysts: A review, *Carbon*, 2021, **172**, 682–711.

16 M. Tan, C. Yu, J. Li, Y. Li, C. Tao and C. Liu, *et al.*, Engineering of g-C_3N_4-based photocatalysts to enhance hydrogen evolution, *Adv. Colloid Interface Sci.*, 2021, **295**, 102488.

17 R. Biswas, P. Thakur, G. Kaur, S. Som, M. Saha and V. Jhajhria, *et al.*, Interfacial Engineering of CuCo 2 S 4/g-C 3 N 4 Hybrid Nanorods for Efficient Oxygen Evolution Reaction, *Inorg. Chem.*, 2021, **60**(16), 12355–12366.

18 U. Ghosh, A. Majumdar and A. Pal, Photocatalytic CO2 reduction over g-C_3N_4 based heterostructures: Recent progress and prospects, *J. Environ. Chem. Eng.*, 2021, **9**(1), 104631.

19 G. Q. Zhao, J. Zou, J. Hu, X. Long and F. P. Jiao, A critical review on graphitic carbon nitride (g-C_3N_4)-based composites for environmental remediation, *Sep. Purif. Technol.*, 2021, **279**, 119769.

20 H. Li, L. Zang, F. Shen, L. Wang, L. Sun and F. Yuan, Tubular g-C 3 N 4/carbon framework for high-efficiency photocatalytic degradation of methylene blue, *RSC Adv.*, 2021, **11**(30), 18519–18524.

21 S. Patnaik, D. P. Sahoo and K. Parida, Recent advances in anion doped g-C_3N_4 photocatalysts: A review, *Carbon*, 2021, **172**, 682–711.

22 Y. Zheng, Y. Liu, X. Guo, Z. Chen, W. Zhang and Y. Wang, *et al.*, Sulfur-doped g-C_3N_4/rGO porous nanosheets for highly efficient photocatalytic degradation of refractory contaminants, *J. Mater. Sci. Technol.*, 2020, **41**, 117–126.

23 J. Wang, G. Wang, B. Cheng, J. Yu and J. Fan, Sulfur-doped g-C_3N_4/TiO2 S-scheme heterojunction photocatalyst for Congo Red photodegradation, *Chin. J. Catal.*, 2021, **42**(1), 56–68.

24 X. Xiao, Y. Wang, Q. Bo, X. Xu and D. Zhang, One-step preparation of sulfur-doped porous g-C 3 N 4 for enhanced visible light photocatalytic performance, *Dalton Trans.*, 2020, **49**(24), 8041–8050.

25 N. Basavaraj, A. Sekar and R. Yadav, Review on green carbon dot-based materials for the photocatalytic degradation of dyes: fundamentals and future perspective, *Mater. Adv.*, 2021, **2**(23), 7559–7582.

26 Y. Duan, S. Zhou, L. Deng, Z. Shi, H. Jiang and S. Zhou, Enhanced photocatalytic degradation of sulfadiazine via g-C_3N_4/carbon dots nanosheets under nanoconfinement: Synthesis, Biocompatibility and Mechanism, *J. Environ. Chem. Eng.*, 2020, **8**(6), 104612.

27 S. Asadzadeh-Khaneghah and A. Habibi-Yangjeh, g-C_3N_4/carbon dot-based nanocomposites serve as efficacious photocatalysts for environmental purification and energy generation: A review, *J. Cleaner Prod.*, 2020, **276**, 124319.

28 F. Wang, P. Chen, Y. Feng, Z. Xie, Y. Liu and Y. Su, *et al.*, Facile synthesis of N-doped carbon dots/g-C_3N_4 photocatalyst with enhanced visible-light photocatalytic activity for the degradation of indomethacin, *Appl. Catal., B*, 2017, **207**, 103–113.

29 P. Malik, S. Duhan and R. Malik, A high-performance humidity sensor based on 3D porous SnO_2 -encapsulated MCM-48 for real-time breath monitoring and contactless gesture detection, *Mater. Adv.*, 2024, **5**(6), 2510–2525.

30 B. Rohilla, A. Boora, M. S. Goyat and S. Duhan, Exploring 2D hexagonal WO 3/COK-12 nanostructures for efficient humidity detection, *Mater. Adv.*, 2023, **4**(22), 5785–5796.

31 L. Ai, R. Shi, J. Yang, K. Zhang, T. Zhang and S. Lu, Efficient Combination of g-C_3N_4 and CDs for Enhanced Photocatalytic Performance: A Review of Synthesis, Strategies, and Applications, *Small*, 2021, **17**(48), 2007523.

32 H. Liu, J. Liang, S. Fu, L. Li, J. Cui and P. Gao, *et al.*, N doped carbon quantum dots modified defect-rich g-C_3N_4 for enhanced photocatalytic combined pollutions degradation and hydrogen evolution, *Colloids Surf., A*, 2020, **591**, 124552.

33 S. Narwal, A. Sura, A. Singh, M. Azam, M. Alam and S. Duhan, *et al.*, *In situ* fabrication of N-doped carbon dots on novel blue-emitting Y_2TiWO_8: Ce^{3+} nanophosphor for thermal sensing and fingerprint detection applications, *Carbon*, 2024, **219**, 118768.

34 L. Cao, R. Wang and D. Wang, Synthesis and characterization of sulfur self-doped g-C 3 N 4 with efficient visible-light photocatalytic activity, *Mater. Lett.*, 2015, **149**, 50–53.

35 S. Cheng, N. Su, P. Zhang, Y. Fang, J. Wang and X. Zhou, *et al.*, Coupling effect of $(SCN)_x$ nanoribbons on PCN nanosheets in the metal-free 2D/1D van der Waals heterojunction for boosting photocatalytic hydrogen evolution from water splitting, *Sep. Purif. Technol.*, 2023, **307**, 122796.

36 K. Li, F. Y. Su and W. D. Zhang, Modification of g-C_3N_4 nanosheets by carbon quantum dots for highly efficient photocatalytic generation of hydrogen, *Appl. Surf. Sci.*, 2016, **375**, 110–117.

37 J. Xu, L. Zhang, R. Shi and Y. Zhu, Chemical exfoliation of graphitic carbon nitride for efficient heterogeneous photocatalysis, *J. Mater. Chem. A*, 2013, **1**(46), 14766.

38 A. F. Shaikh, M. S. Tamboli, R. H. Patil, A. Bhan, J. D. Ambekar and B. B. Kale, Bioinspired Carbon Quantum Dots: An Antibiofilm Agents, *J. Nanosci. Nanotechnol.*, 2019, **19**(4), 2339–2345.

39 L. Ge, C. Han, X. Xiao, L. Guo and Y. Li, Enhanced visible light photocatalytic hydrogen evolution of sulfur-doped polymeric g-C_3N_4 photocatalysts, *Mater. Res. Bull.*, 2013, **48**(10), 3919–3925.

40 Z. Xu, Y. Wang, J. Zhuang, Y. Li and L. Jia, High temperature hydrothermal etching of g-C_3N_4 for synthesis of N doped carbon quantum dots-supported CdS photocatalyst to enhance visible light driven hydrogen generation, *Mol. Catal.*, 2022, **517**, 111900.

41 Y. Wang, X. Liu, J. Liu, B. Han, X. Hu and F. Yang, *et al.*, Carbon Quantum Dot Implanted Graphite Carbon Nitride Nanotubes: Excellent Charge Separation and Enhanced Photocatalytic Hydrogen Evolution, *Angew. Chem., Int. Ed.*, 2018, **57**(20), 5765–5771.

42 Y. Wang, X. Liu, J. Liu, B. Han, X. Hu and F. Yang, *et al.*, Carbon Quantum Dot Implanted Graphite Carbon Nitride Nanotubes: Excellent Charge Separation and Enhanced Photocatalytic Hydrogen Evolution, *Angew. Chem., Int. Ed.*, 2018, **57**(20), 5765–5771.

43 H. Diarmand-Khalilabad, A. Habibi-Yangjeh, D. Seifzadeh, S. Asadzadeh-Khaneghah and E. Vesali-Kermani, g-C_3N_4 nanosheets decorated with carbon dots and CdS nanoparticles: Novel nanocomposites with excellent nitrogen photofixation ability under simulated solar irradiation, *Ceram. Int.*, 2019, **45**(2), 2542–2555.

44 A. Singh, V. Kaushik, S. Chahal, A. Goswami and S. Nain, Efficient Degradation of Methylene Blue Dye and Antibacterial Performance of Shape Controlled RuO 2 Nanocomposites, *ChemistrySelect*, 2021, **6**(37), 10038–10050.

45 J. Xu, Z. Wang and Y. Zhu, Enhanced Visible-Light-Driven Photocatalytic Disinfection Performance and Organic Pollutant Degradation Activity of Porous g-C_3N_4 Nanosheets, *ACS Appl. Mater. Interfaces*, 2017, **9**(33), 27727–27735.

46 A. Singh, A. Goswami and S. Nain, Enhanced antibacterial activity and photo-remediation of toxic dyes using Ag/SWCNT/PPy based nanocomposite with core–shell structure, *Appl. Nanosci.*, 2020, **10**(7), 2255–2268.

47 Z. Xie, Y. Feng, F. Wang, D. Chen, Q. Zhang and Y. Zeng, *et al.*, Construction of carbon dots modified MoO_3/g-C_3N_4 Z-scheme photocatalyst with enhanced visible-light photocatalytic activity for the degradation of tetracycline, *Appl. Catal., B*, 2018, **229**, 96–104.

48 H. Chen, X. Zhang, L. Jiang, X. Yuan, J. Liang and J. Zhang, *et al.*, Strategic combination of nitrogen-doped carbon quantum dots and g-C_3N_4: Efficient photocatalytic peroxydisulfate for the degradation of tetracycline hydrochloride and mechanism insight, *Sep. Purif. Technol.*, 2021, **272**, 118947.

49 W. Shi, S. Yang, H. Sun, J. Wang, X. Lin and F. Guo, *et al.*, Carbon dots anchored high-crystalline g-C_3N_4 as a metal-free composite photocatalyst for boosted photocatalytic degradation of tetracycline under visible light, *J. Mater. Sci.*, 2021, **56**(3), 2226–2240.

50 A. Iqbal, F. B. Shittu, M. N. M. Ibrahim, N. H. H. A. Bakar, N. Yahaya and K. Rajappan, *et al.*, Photoreactive Carbon Dots Modified g-C_3N_4 for Effective Photooxidation of Bisphenol-A under Visible Light Irradiation, *Catalysts*, 2022, **12**(11), 1311.

51 C. Xavier, B. R. Lopes, C. Lima, S. de, C. Ribeiro and E. B. Azevedo, Using a Surface-Response Approach to Optimize the Photocatalytic Activity of rGO/g-C_3N_4 for Bisphenol A Degradation, *Catalysts*, 2023, **13**(7), 1069.

52 A. Uddin, A. Rauf, T. Wu, R. Khan, Y. Yu and L. Tan, *et al.*, In_2O_3/oxygen doped g-C_3N_4 towards photocatalytic BPA degradation: Balance of oxygen between metal oxides and doped g-C_3N_4, *J. Colloid Interface Sci.*, 2021, **602**, 261–273.

53 R. Verma and S. K. Samdarshi, In Situ Decorated Optimized CeO 2 on Reduced Graphene Oxide with Enhanced Adsorptivity and Visible Light Photocatalytic Stability and Reusability. The, *J. Phys. Chem. C*, 2016, **120**(39), 22281–22290.

54 P. K. Sanoop, S. Anas, S. Ananthakumar, V. Gunasekar, R. Saravanan and V. Ponnusami, Synthesis of yttrium doped nanocrystalline ZnO and its photocatalytic activity in methylene blue degradation, *Arabian J. Chem.*, 2016, **9**, S1618–S1626.

55 L. Bai, R. Guo, Z. Chen, L. Liu, G. Dong and J. Zhang, *et al.*, Chemically fabricated ZnO/Ag/Ag Mo O/Zn Mo O heterojunction nanophotocatalysts for abating organic dyes in wastewater, *J. Cleaner Prod.*, 2022, **363**, 132481.

56 Y. Wang, X. Li, W. Lei, B. Zhu and J. Yang, Novel carbon quantum dot modified g-C_3N_4 nanotubes on carbon cloth for efficient degradation of ciprofloxacin, *Appl. Surf. Sci.*, 2021, **559**, 149967.

57 H. Liu, J. Liang, S. Fu, L. Li, J. Cui and P. Gao, *et al.*, N doped carbon quantum dots modified defect-rich g-C_3N_4 for enhanced photocatalytic combined pollutions degradation and hydrogen evolution, *Colloids Surf., A*, 2020, **591**, 124552.

58 Y. Wang, Y. Li, J. Zhao, J. Wang and Z. Li, g-C_3N_4/B doped g-C_3N_4 quantum dots heterojunction photocatalysts for hydrogen evolution under visible light, *Int. J. Hydrogen Energy*, 2019, **44**(2), 618–628.

59 S. Patial, Sonu, A. Sudhaik, N. Chandel, T. Ahamad and P. Raizada, *et al.*, A Review on Carbon Quantum Dots Modified g-C_3N_4-Based Photocatalysts and Potential Application in Wastewater Treatment, *Appl. Sci.*, 2022, **12**(21), 11286.

60 H. Chen, X. Zhang, L. Jiang, X. Yuan, J. Liang and J. Zhang, *et al.*, Strategic combination of nitrogen-doped carbon quantum dots and g-C_3N_4: Efficient photocatalytic peroxydisulfate for the degradation of tetracycline hydrochloride and mechanism insight, *Sep. Purif. Technol.*, 2021, **272**, 118947.

61 F. Mahdipour, M. Rafiee, B. Kakavandi, Z. Khazaee, F. Ghanbari and K. Y. Andrew Lin, *et al.*, A new approach on visible light assisted oxygen doped g-C_3N_4/β-Bi_2O_3 direct Z-scheme heterojunction towards the degradation of bisphenol A: Degradation pathway, toxicity assessment, and continuous mode study, *Sep. Purif. Technol.*, 2022, **303**, 122171.

62 X. He, T. Kai and P. Ding, Heterojunction photocatalysts for degradation of the tetracycline antibiotic: a review, *Environ. Chem. Lett.*, 2021, **19**(6), 4563–4601.